

Glutathione-magnetite nanoparticles: synthesis and physical characterization for application as MRI contrast agent

J. J. Beato-López¹  · M. Domínguez² · M. Ramírez-del-Solar² · R. Litrán²

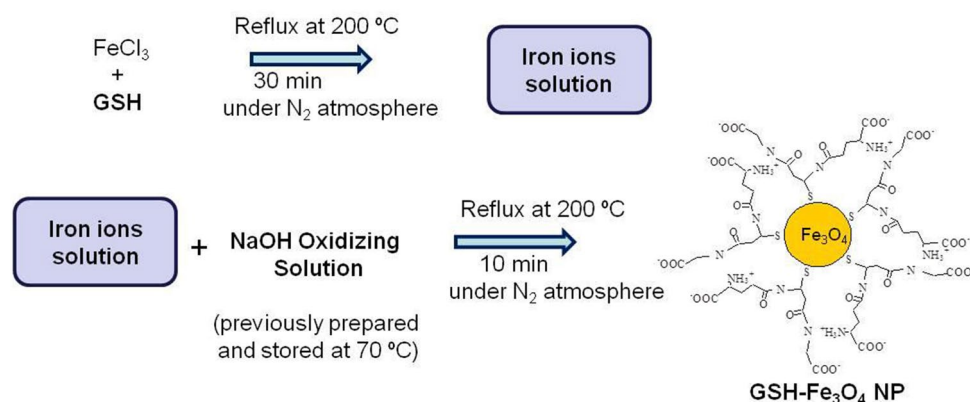
Received: 21 January 2020 / Accepted: 8 June 2020 / Published online: 12 June 2020

© Springer Nature Switzerland AG 2020

Abstract

In this work a one-pot synthesis of water soluble glutathione capped magnetite nanoparticles is reported. The magnetic characterization of the samples shows the expected superparamagnetic behavior, but a wide range of blocking temperatures is found, since the size and interparticle interactions are very sensitive to preparation conditions. These properties are correlated with the glutathione-iron ratio and oxidant dose, in order to optimize the aqueous colloidal stability and magnetic properties of the superparamagnetic iron oxide nanoparticles for Magnetic Resonance Imaging applications. The efficiency of the glutathione coated nanoparticles as contrast agent is then evaluated by means of the determination of the relaxation times T₁ and T₂ in ¹H Nuclear Magnetic Resonance experiments. Moreover, the influence of the thickness of the glutathione capping layer on the colloidal stability and, thus, on relaxation times has been studied. Finally, the relaxivity of the sample that shows the best performance has been determined.

Graphic abstract A novel *one-pot synthesis* for “in situ” functionalized hydrophilic magnetite nanoparticles at atmospheric pressure and a temperature lower than 200 °C for Magnetic Resonance Imaging applications is reported. Their properties are analyzed in terms of the synthesis process: glutathione-iron ratio and oxidant dose.



Keywords Magnetic nanoparticle · Superparamagnetism · MRI contrast agent · Colloidal solubility · Nanoparticle interaction · Glutathione

Mathematical Subject Classification 82D80

✉ J. J. Beato-López, juanjesus.beato@unavarra.es | ¹Departamento de Ciencias, Edificio de los Acebos, Universidad Pública de Navarra and Institute for Advanced Materials (INAMAT2), Campus de Arrosadia, 31006 Pamplona, Spain. ²Departamento de Física de la Materia Condensada and Instituto de Microscopía Electrónica y Materiales (IMEYMAT), Universidad de Cádiz, Puerto Real (Cádiz), Spain.



SN Applied Sciences (2020) 2:1202 | <https://doi.org/10.1007/s42452-020-3010-y>

1 Introduction

Magnetic nanoparticles (NPs) have been widely investigated and utilized in the last decades [1–4], due to their different applications in different fields such as, biotechnology [5], catalysis [6], wastewater treatment [7], optoelectronic [8] and biomedicine [9, 10]. Specifically, in the field of biomedicine, applications for protein immobilization [11], as hyperthermia agents for cancer therapy [12, 13], for drug delivery [3], and as contrast agents for Magnetic Resonance Imaging (MRI) [14–17] has been proposed. Particularly, iron oxides, and especially magnetite (Fe_3O_4) NPs, are the most commonly used due to their biocompatibility, low cytotoxicity and stability.

Magnetic Resonance Imaging (MRI) is a non-invasive clinical diagnostic technique with a high spatial resolution that is extensively used for anatomical imaging of soft body tissues [17, 18]. In recent years, MRI has been used for tracking and monitoring cells in vivo [19]. However, this technique requires the use of contrast agent to enhance the differences between damage and normal tissues. In the case of tracking applications, cells must also be labeled with these MRI contrast agents. Small molecular paramagnetic gadolinium complexes have been extensively used for positive contrast, because these complexes act as longitudinal relaxation time (T_1) contrast agents [18]. In this sense, improved relaxivities rates ($r_i = 1/T_i; i = 1, 2$) have been reported for Gd complexes confined into porous media [20]. Anyway, the possibility to use other systems based on polymers [21], micelles [22] and hydrogels [23] have been studied in order to improve the technique, increasing the contrast, the sensibility and the duration of the signal for long-term in vivo measurements [18].

On the contrary, superparamagnetic iron oxide nanoparticles (SPIONs) are used in MRI as transverse relaxation time (T_2) contrast agents since, in addition to their low toxicity and biocompatibility, they show excellent magnetic properties [24–27]. Specifically, the presence of SPIONs shortens the transverse relaxation time of surrounding water protons, leading to a decrease of the MRI signal (negative contrast agents). Normally, NPs biomedical applications require a high hydrophilic character together with the possibility of their conjugation with biological species [18, 28]. Additionally, the colloidal stability of SPIONs may constrain their applications in MRI. For this application, NPs are required to show aqueous stability, high crystallinity and a narrow size distribution. If SPIONs are appropriately coated, hydrophilic and stable NPs can be obtained, preserving their superparamagnetic behavior. The correct functionalization process increases the colloidal stability of SPIONs and, consequently, enhances its possibilities as MRI contrast agents [29]. Therefore, this

functionalization allows for the subsequent bioconjugation and aids in preventing SPIONs toxicity [30–33].

We have previously reported [34] about the cytotoxicity of different NPs coated with glutathione (GSH), a tripeptide that bounds the NP surface by means of the thiol group contained in its structure. Even in the case of Quantum dots (QDs) with a potential toxic core, we concluded that there was no significant increase in cellular death when NP was present, due to the GSH entirely covers the surface of the NP. On the other hand, we have also reported the efficiency of GSH capping demonstrating that, after capping, the GSH molecule retains the capability of linking to biological species and also the ability for specifically links [35, 36].

The purpose of the present work it is to obtain highly stable magnetite NPs in aqueous medium by using GSH as stabilizing specie, due to its hydrophilic and biocompatible character. Although several different one pot synthetic routes have been proposed to prepared water soluble magnetite nanoparticles, in this work we present a one pot facile route based on a precipitation reaction at relatively low temperature and at atmospheric pressure, to obtain directly functionalized magnetite NPs. These NPs are “in situ” capped with GSH, a biocompatible molecule with amino and carboxylic terminal groups for subsequent crosslinking processes [37–39]. The influence of synthesis additives on the size and polydispersivity of the NPs and thus, on the magnetic properties of magnetite NPs, is studied. Finally, for the application proposed, the efficiency of these SPIONs for T_2 -weighted MRI applications was also evaluated from relaxation Nuclear Magnetic Resonance (NMR) experiments.

2 Experimental

2.1 Synthesis of NPs

For the preparation of SPIONs we have designed a synthesis method based on the thermal decomposition of an iron salt, in the presence of a hydrophilic capping species to functionalize the NP and to control its final size. All the chemicals, iron (III) chloride (FeCl_3), sodium hydroxide (NaOH), diethylene glycol and reduced glutathione (GSH), were purchased from Sigma-Aldrich (analytic grade), and used as received. MilliQ water was used for all experiments.

The synthesis of GSH- Fe_3O_4 NPs was carried out in two steps. The first step consisted on the main thermal decomposition reaction. In brief, 0.55 g of FeCl_3 , used as iron precursor, was dissolved into 15 ml of diethylene glycol, used as solvent. The obtained solution was then placed in a 500 ml three-necked flask, where the GSH used as capping

agent was added. Different GSH:Fe molar ratios have been used (1:6; 1:7,5; 1:9 and 1:14), in order to study the influence of the GSH proportion on size and on magnetic properties of the final magnetite NPs. The solution was heated at 200 °C under reflux in a nitrogen atmosphere, in order to promote the thermal decomposition of iron salt.

In a second step, after heating the above solution under reflux for 30 min, an oxidizing agent is added to promote the controlled co-precipitation and formation of magnetite NPs. As oxidizing agent, we have used a NaOH solution, previously prepared by heating 20 g of NaOH and 20 ml of diethylene glycol at 120 °C under reflux in a nitrogen atmosphere for 1 h. After this time, the solution is cooled at 70 °C and stored at this temperature to be added to the solution containing the iron precursor. Different volumes (4, 8 and 10 ml) of this NaOH solution, stored at 70 °C, have been used to study the effect of its concentration on the NPs properties. Once the NaOH was added, the total solution was heated for 10 min, keeping the temperature at 200 °C.

After cooled at room temperature, the obtained solution was filtered three times (using a 0.1 μ Millipore membrane), after precipitation with ethanol, in order to eliminate the excess of precursor species and/or residues from

the reaction present. As result, we obtained Fe₃O₄ NPs capped with GSH molecules (GSH-Fe₃O₄ NPs) that can be easily solved in aqueous solution due to the hydrophilic character conferred by the GSH moiety. The experimental procedure is schematized in Fig. 1:

As mentioned before, different series of samples were obtained by changing: the Fe:GSH ratio (from 1:6 to 1:14) and the volume of NaOH oxidizing solution (4, 8 and 10 ml). For the sake of clarity, samples were labelled (as shown in Table 1) as a function of experimental parameters through the code GXY, where X refers to the added GSH moles per mol of Fe and Y represents the volume of NaOH, L, M and H being 4, 8 and 10 mL, respectively.

2.2 Characterization

Structure and chemical composition of the NPs were first inspected. Crystalline Phase identification of nanoparticles was performed by X-Ray Diffraction (XRD) in a Bruker D8 Advance diffractometer using CuKα radiation in the 15–65° angular range. Crystallite average sizes were evaluated from the main magnetite (311) diffraction peak, by using the Scherrer formula with constant K=0.94. In order to take into account the size distribution, calculations were

Fig. 1 Experimental synthesis procedure for the preparation of GSH-Fe₃O₄ NPs

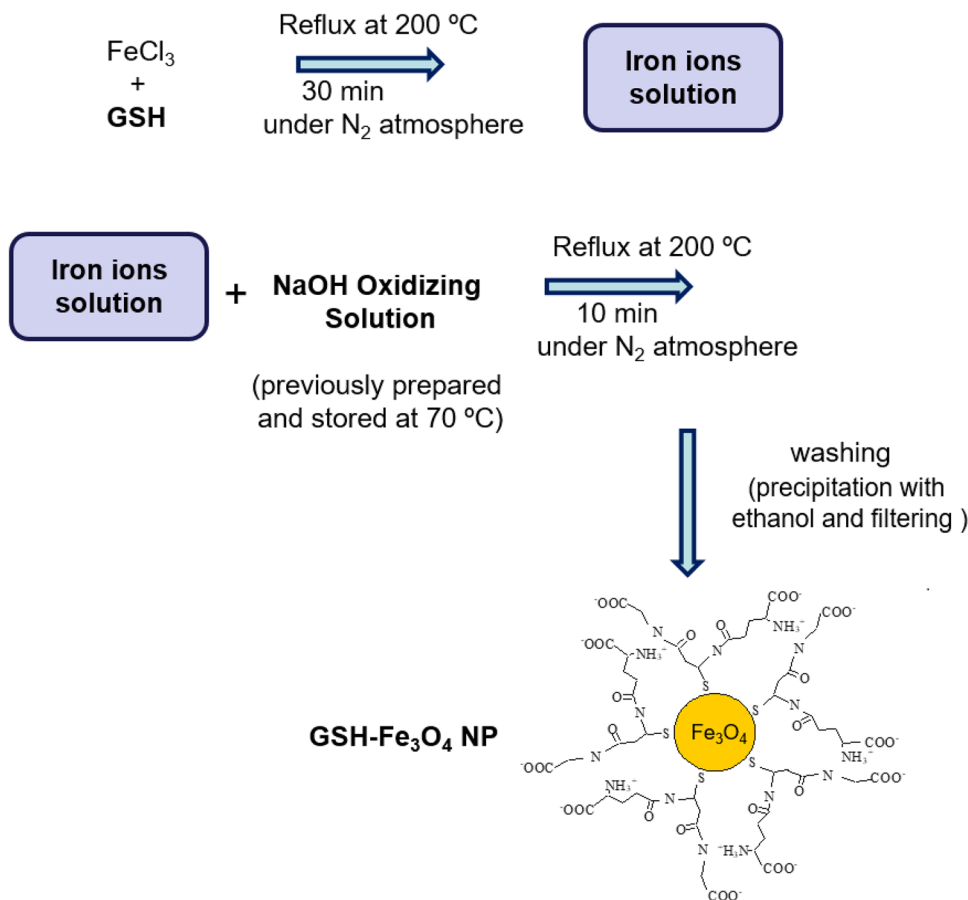


Table 1 Codes used to name the NPs samples prepared and the corresponding synthesis conditions: GSH:Fe molar ratio and the NaOH volume used for the oxidation reaction

NaOH volume	Fe:GSH molar ratio	Sample code
Low (4 ml)	1:6	G6L
	1:7.5	G7.5L
	1:9	G9L
Medium (8 ml)	1:7.5	G7.5 M
	1:9	G9M
	1:14	G14M
High (10 ml)	1:9	G9H
	1:14	G14H

performed from the integral breath, considering the width of a square topped profile with the same total area and height. ICP (Inductively Coupled Plasma-atomic emission spectrometry) analyses have been performed in order to determine the iron content of NPs.

The shape, size and distribution of NPs were studied from images taken by Transmission Electron Microscopy (TEM), using a JEOL2011, and Atomic Force Microscopy (AFM), using a Veeco Multimode Nanoscope IIIa microscope in tapping mode with antimony (n) doped Si probes (Bruker RTESP), in air. A similar procedure was followed for the sample preparation in both techniques. Initially, the NPs were dispersed in MQ water. Different concentrations of solutions were prepared to study its effect on image quality correspondingly. Then, the optimal solution was subjected to sonication for 15 min to improve the dispersion of the particles in the solution and avoiding aggregation. Finally, a single drop was deposited into a holey carbon copper grid and a freshly cleaved mica substrate for TEM (10 μ L) and AFM (50 μ L) analysis respectively. Finally, a similar drying process was performed for both techniques by heating at 50 °C in air. Tens of micrographs around the whole grid area (similar to those shown in Fig. 3) were employed in the TEM diameter size analysis. The nanoparticle size estimation was performed by using the free software Digital Micrograph. A standard procedure based on the estimation of NPs diameter through the correlation with the known size of the scale bar in every analyzed picture was followed. No less than 100 hundred nanoparticles were analyzed per sample. Regarding to AFM analysis, the free software Gwyddion [40] was used for the analysis of the images, starting with the correction of any artifacts. Then, the nanoparticles were marked with a mask, setting a threshold height of 2 nm and rejecting any particle appearing close to image edges. Once the nanoparticles are located in the AFM images, the statistics of their equivalent diameter of the nanoparticles (considering them as spherical and so, circles in the 2D image) were obtained using the tool “grain distribution”, also provided by

the software Gwyddion. A total number of 20 images (scan size $1 \times 1 \mu\text{m}^2$) were used in the analysis of sample G9M and 410 nanoparticles were thus counted.

The hydrodynamic size of optimal samples, as well as the Z-Potential value, were studied by Dynamic Light Scattering (DLS) technique by a Zeta Nanosizer using a 1 cm path cell, at 25 °C. The samples behavior was measured in a colloidal PBS solution.

Magnetic properties of the synthesized nanoparticles were checked by the measurement of the magnetization curves at room temperature (Oxford Instruments Magnetic Faraday Balance) and the ZFC-FC (zero field cooled/field cooled) curves (Vibrating Sample Magnetometer Form Cryogenic Ltd.).

$^1\text{H-NMR}$ (Nuclear Magnetic Resonance) experiments were performed at 25 °C in a field of 14.1T from a Varian Agilent 600 with 5 mm probes. The Larmor frequency for ^1H was 600 MHz. For a preliminary assessment of the potential of iron oxide nanoparticles (IONP) as MRI contrast agents, the longitudinal (T_1) and transverse (T_2) relaxation times were measured for each sample. For T_1 determination, a standard inversion recovery (IR) pulse sequence was used with a 180° square RF pulse followed by a RF 90° after a characteristic time (inversion time, TI) to record the magnetization recovery. T_1 was calculated from the evolution of the proton signal along the static field for different inversion times (50–6400 ms) which characterize the spin-lattice relaxation.

$$M_z(t) = M_z(0) \left(1 - 2e^{-\left(\frac{t}{T_1}\right)} \right) \quad (1)$$

For T_2 determination, a multi-echo spin echo CPMG sequence (Carr-Purcell-Meiboom-Gill [41]) was used with a π pulse in xy plane after the 90° pulse, which leads to spin refocusing and echo formation. Neglecting pulse imperfections, the echo tops will diminish in intensity due to coherence losses between spins, that is, spin-spin relaxation characterized by T_2 . The π pulses refocus the inhomogeneous T_2 (T_2^*) related to the varying magnetic field experienced by the sample and other non-random effects. So the spin-spin relaxation follows an exponential decrease:

$$M_{xy}(t) = M_{xy}(0) e^{-\left(\frac{t}{T_2}\right)} \quad (2)$$

For this measurement, a relevant parameter is the echo time (TE) elapsed from the RF 90° -pulse until the echo. Two different values of TE were used, typically 1 and 2 ms.

3 Results and discussion

3.1 Structural characterization

As mentioned above, we have evaluated the effect of two synthesis parameter on the morphological and structural characteristics of the NPs obtained dose. Specifically, Fe:GSH molar ratio and oxidizing agent dose were examined. First, the effectiveness of the oxidation process, that takes place on the formation of magnetite crystalline phase, was evaluated by using different volumes of NaOH solution. Figure 2 shows the XRD patterns obtained at room temperature, for G6L, G9M and G14 H, respectively. It can be noticed that, all the studied samples present the characteristic diffraction peaks of magnetite phase at 35.5° (311), 62.6° (440), 57.0° (511), 30.1° (220), 43.1° (400). However, it was observed that, as increasing the dose of oxidizing agent, peaks become more intense

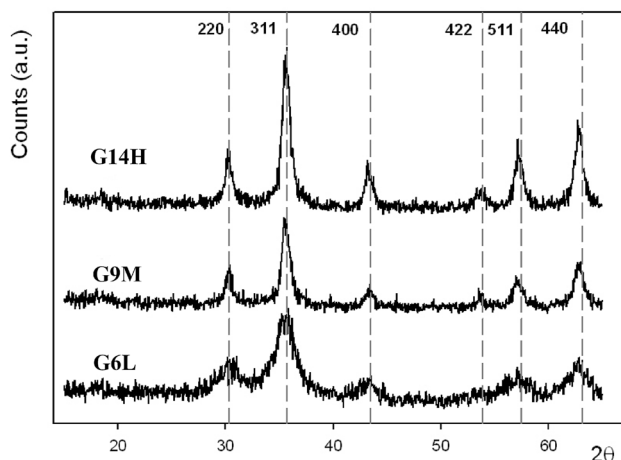


Fig. 2 XRD patterns registered at room temperature, for samples G6L, G9M and G14 H. Diffraction angles corresponding to magnetite phase are marked with dash lines

Table 2 Magnetite MGT and GSH weight percentages obtained from ICP analysis and the estimated percentages by the simplified model described in the text are shown

Sample	% MGT ICP	% MGT (estimated)	% GSH ICP	% GSH (estimated)	D_{TEM} (nm)	D_{XRD} (nm)	D_{BF} (nm)	D_{ZFC} (nm)
G6L	67.99	68.35	32.01	31.65	3.9 ± 0.2	5.3	4.46	4.24
G7.5L	63.29	63.60	36.71	36.40	3.2 ± 0.2		5.23	
G9L	67.03	65.58	32.97	34.42	3.5 ± 0.2		3.87	
G7.5 M	70.62	77.56	29.38	22.44	5.8 ± 0.7		5.96	
G9M	57.21	78.18	42.79	21.82	6.0 ± 0.9	9.1	6.87	6.56
G14M	67.58	78.32	32.42	21.68	6.1 ± 0.8		8.35	
G9H	41.18	75.53	58.82	24.47	5.3 ± 0.5		6.29	
G14 H	71.72	84.30	28.28	15.70	8.8 ± 1.2	9.2	9.91	9.70

Average NP sizes evaluated from TEM micrographs (D_{TEM}), XRD patterns (D_{XRD}) and calculated from magnetic measurements (D_{BF} and D_{ZFC}) are also shown

and narrower. This effect can be associated to the presence of greater nanocrystals and it is particularly remarkable when increasing the NaOH dose from L to M. Alkaline condition (for pH value close to 10) is preferred during synthesis as it can provide electrons. The fast addition of NaOH is crucial to provide hydroxyl groups, provoking the formation of homogeneous magnetite nuclei. However, larger particle size resulted from adding excess of NaOH [38]. The excess alkalinity provided by the hydroxide ions promoted the acceleration of hydrolysis, leading to the growth of magnetite NP cores [42]. This can be the reason for the increase in the NP diameter when the oxidizing dose is increased from L (4 mL) to M (8 mL). There is not a clear influence of the NaOH concentration on the NP size for concentrations higher than 8 mL, probably already in excess. Besides, as can be seen from Table 2, larger crystallite sizes are obtained from XRD patterns than those evaluated from TEM images. This can be justified by the fact that the evaluation from the XRD peak width is most affected by the largest crystals, being a volume average size while the analysis by TEM is number average size [43].

The percentage of iron was evaluated through ICP technique and, assuming that magnetite is the only existing crystalline iron oxide phase, the magnetite fraction (% MGT ICP), shown in Table 2, was calculated. The GSH content of the capped NPs (% GSH ICP) is around 30–40% in most of the samples, with a no straightforward dependence on the processing parameters.

The morphology of MGT NPs was inspected by TEM (Fig. 3). As it can be observed, the higher atomic weight of iron gives a good contrast and the concentration of NPs enables a statistical count of the size distribution. In this sense, micrographs reveal the formation of relatively small nanocrystals with homogeneous size distributions that are well fitted to a Gaussian function (Fig. 3), whose peak position and variance depend on both the amount of NaOH and proportion of GSH (see Table 2). A clear increment in NP average size is observed when the volume of added

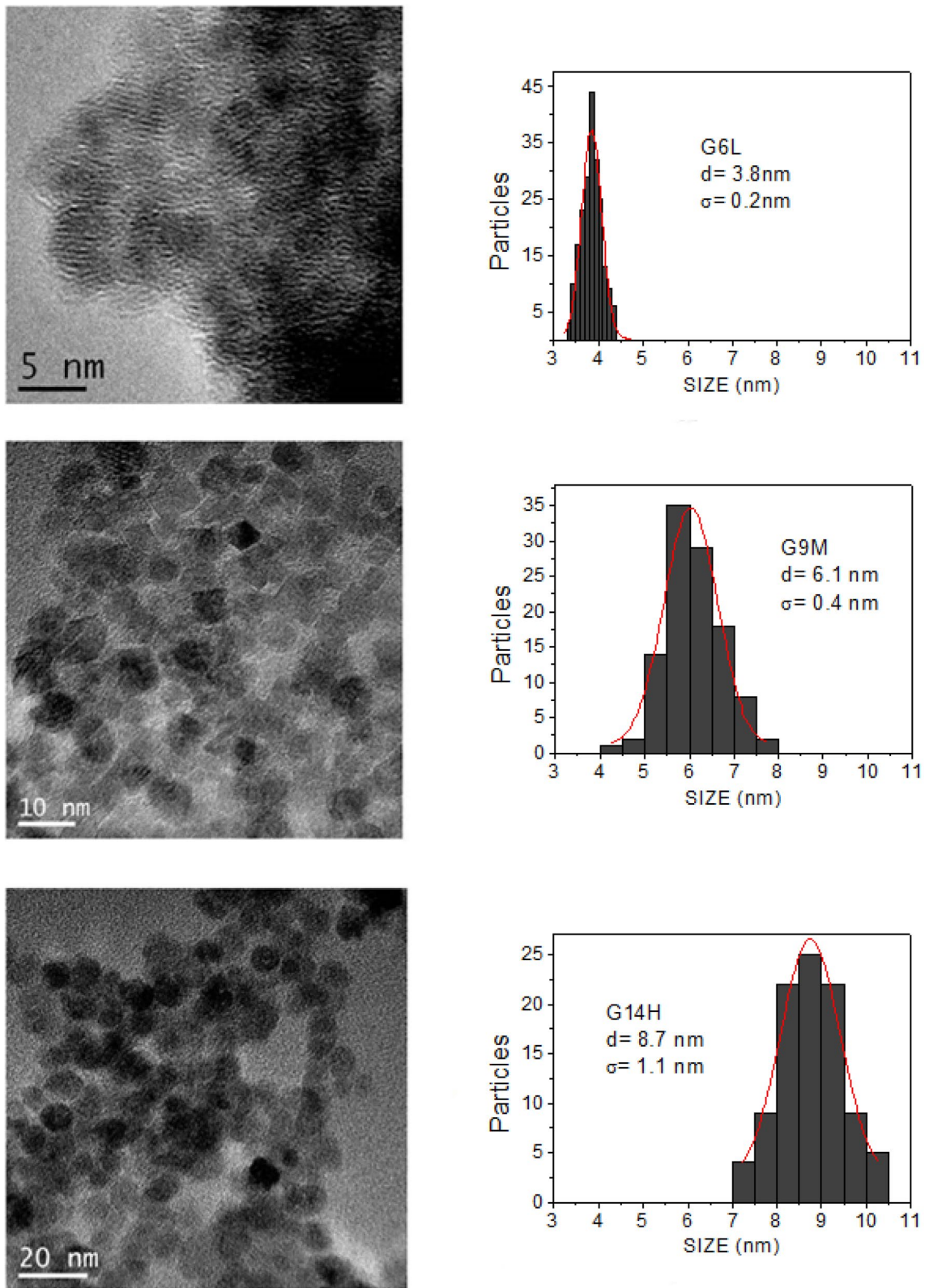


Fig. 3 TEM micrographs obtained for G6L, G9M and G14H samples, as well as their corresponding Np size histograms. Continuous lines correspond to the best fitting Gaussian functions of the size distributions

NaOH is increased from low (3.2–3.8 nm) to medium (5.8–6.1 nm). In these cases, no net effect in size of GSH molar ratio is noticed. A further increase in NP size is only achieved under a larger NaOH volume (10 mL) and lower GSH:Fe molar ratio (8.8 nm), showing that this combination results in the highest NP average size and wider size distribution. The width of the distributions follows a similar behavior. In fact, samples for Fig. 3 were chosen as representative for one of the three size ranges that we have obtained.

These TEM NPs sizes can be used for the estimation of the number of GSH molecules surrounding the magnetic core. With this purpose, a simple model described elsewhere [35] is employed. This model is based on the assumption of a spherical Fe_3O_4 core covered by a single layer of GSH molecules linked through the thiol group and forming a spherical crown of variable density. Thus, the estimated values of the GSH percentage, shown in Table 2 (% GSH (estimated)), can be compared to the experimental ICP values and, then, the deviation from this GSH monolayer model can be inferred. For the smallest NPs, we found a good agreement between experimental and calculated GSH percentages, confirming the validity of this GSH monolayer model. However, as the NPs size increases, the experimental GSH proportions are considerably higher than those predicted by the model. These deviations can be explained considering that these NPs are surrounded by more than one GSH layer or assuming that the relaxation of steric hindrance in the larger particles allows a higher GSH density in the layer. This increase in the layer GSH density will affect the colloidal stability of the samples as it will be discussed in a following section.

3.2 Magnetic characterization

Magnetic behavior of the samples was initially checked by measuring the magnetization curves at room temperature with the Faraday Balance applying magnetic fields of up to 0.6 T. For the sake of clarity only the magnetization curves of three samples (G6L, G9M and G14H) that covers the full range of size and magnetization values are shown in Fig. 4a. These curves have been fitted to Langevin equation (Eq. 3).

$$M_{SPM} = M_s \left[\coth \left(\frac{\mu_0 M_s V H}{k_B T} \right) - \frac{k_B T}{\mu_0 M_s V H} \right] \quad (3)$$

where M_s is the saturation magnetization, μ_0 is the vacuum magnetic permeability, k_B is Boltzmann constant, V is the volume of the nanoparticles, H the applied magnetic field and T the temperature. To simplify this initial analysis a single average volume has been considered in Eq. 3 and, since the particles are essentially spherical, $V = \pi D^3/6$. The

average diameter values obtained from the fits of Eq. 3 are shown in Table 2 as D_{BF} being, in general, consistent with the values calculated from TEM.

Figures 4b–d show the ZFC/FC magnetization curves for the same samples at 50 Oe ($H \approx 3979$ A/m). These ZFC curves have been fitted to the following function:

$$M_{ZFC} = \int_0^{V_c} M_{SPM} f(V) dV + \int_{V_c}^{\infty} M_{BLQ} f(V) dV \quad (4)$$

by using an iterative method based on the Levenberg–Marquardt algorithm developed with the open source numerical analysis software Scilab [44]. Here, the first term represents the contribution to the total magnetization due to the fraction of NPs which are superparamagnetic (SPM) for each temperature (i.e., those NPs with a volume below a certain critical value [45] $V_c = 25 k_B T/K$, where K is the magnetic anisotropy). The second term sums up the magnetization of NPs fraction that are blocked at each temperature (i.e., those for which $V > V_c$). The volume distribution $f(V)$ is converted to the diameter (size) distribution, $f(D)$, that is supposed to be log-normal and then given by:

$$f(D) = \frac{1}{\sqrt{2\pi}D\beta} \exp \left[\frac{-(\ln D - \ln \alpha)^2}{2\beta^2} \right] \quad (5)$$

The median α and the standard deviation β are the first two free parameters used for the non-linear fitting of $M(T)$ ZFC curves. From these two parameters, the expected value for the diameter of the NPs is given by:

$$\bar{D} = \alpha \exp \left(\frac{\beta^2}{2} \right) \quad (6)$$

And the variance is calculated as:

$$\sigma^2 = \bar{D}^2 \left(\frac{\bar{D}^2}{\alpha^2} - 1 \right) \quad (7)$$

The magnetization of the SPM fraction of NPs in Eq. 4 is given by the Langevin function (Eq. 3). On the other hand, the magnetization for the NPs that are blocked at each temperature is given by the low-field approximation of the Langevin function, equivalent to the Curie law:

$$M_{BLQ} = M_s \left(\frac{\mu_0 M_s H}{3k_B T} \right) \quad (8)$$

It is also supposed that the spontaneous magnetization, M_s , depends on temperature as:

$$M_s(T) = M_s(0)(1 - fT^{3/2}) \quad (9)$$

where f is also a free parameter for the non-linear fitting of the ZFC curves $M(T)$. Finally, to obtain a better fit of these

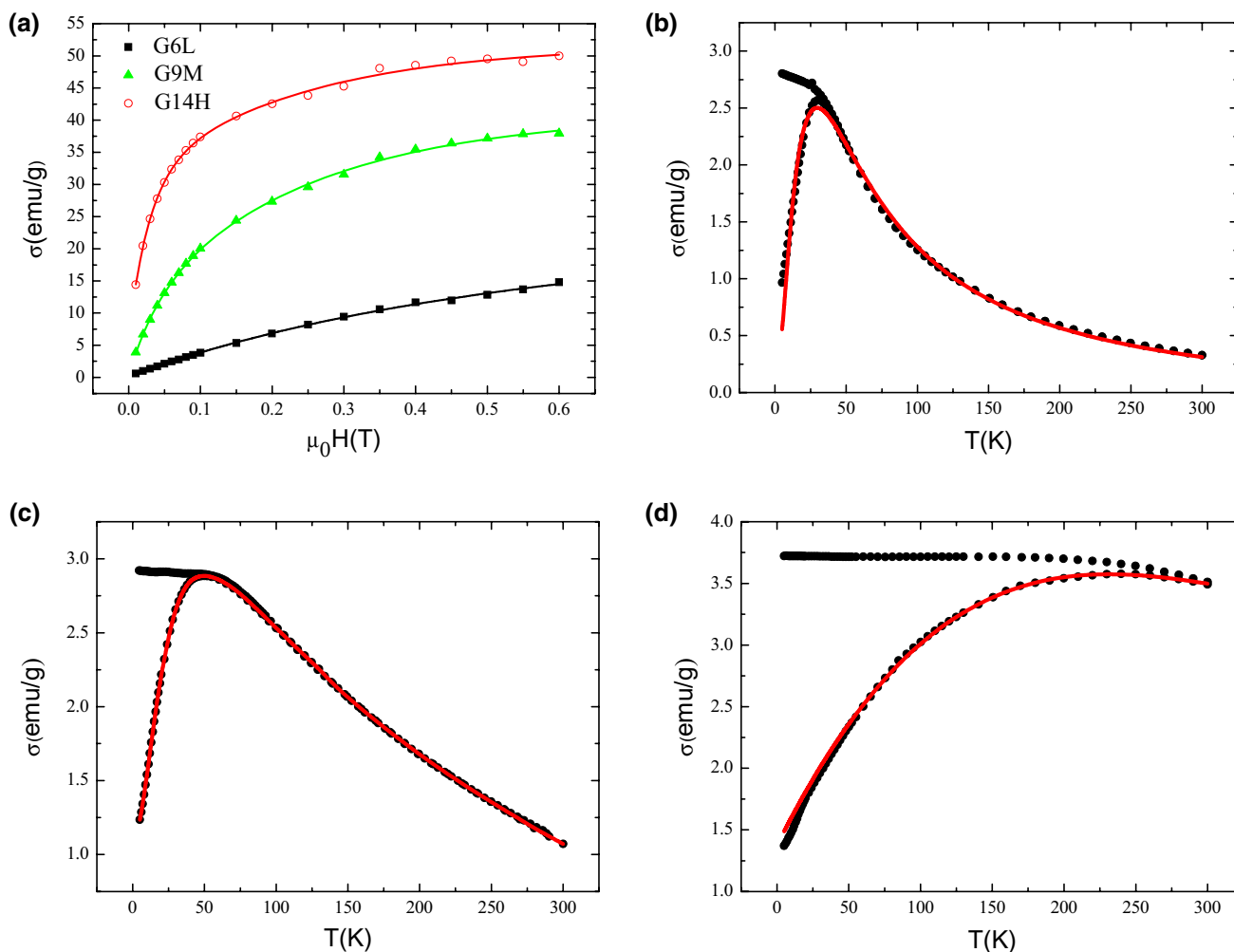


Fig. 4 **a** Magnetization curves of the samples G6L, G9M and G14H at room temperature measured with Faraday Balance. ZFC/FC curves and their respective fitting for the samples: **b** G6L, **c** G9M and **d** G14H

curves, it was necessary to include the dependence of magnetic anisotropy on temperature:

$$K(T) = K(0)(1 - fT^{3/2})^{n(n+1)/2} \tag{10}$$

In this relationship, the coefficient n is 2 for uniaxial anisotropy and 4 for cubic anisotropy. Given the fact that the NPs are made of magnetite, a cubic crystal, one should expect this value to be 4 in our case. However, the ZFC curves are better fitted with a value of $n \approx 2$, probably because of the shape anisotropy (the NPs are not perfectly spherical) that makes them essentially uniaxial, from the point of view of the magnetic anisotropy [46]. This may be understood as a consequence of shape anisotropy. For relatively large nanoparticles, even a small deviation from perfect sphericity would allow the shape anisotropy to dominate over magnetocrystalline anisotropy, since the nanoparticles should be considered as spheroids,

and then, the spontaneous magnetization vector would tend to align at zero field along the larger axis (easy axis) of the oblate or prolate spheroids, following the Stoner-Wohlfarth model [47, 48].

In order to obtain more physically reasonable fitting parameters, as well as the best fitted curves, a 3-step non-linear fitting process was applied for all the ZFC curves studied. In the first step, only the parameters α and β were obtained, while the temperature dependences of the spontaneous magnetization and the magnetic anisotropy (Eqs. 9 and 10) were not considered. In a second step, the temperature dependence of the spontaneous magnetization is taken into account and the value of parameter f is thus obtained, while previously obtained parameters α and β are allowed to change by $\pm 10\%$. Finally, the temperature dependence of the magnetic anisotropy is also considered during the fitting process while previously obtained parameters α , β and f are kept within a $\pm 10\%$

range of their previous values. The values of \bar{D} deduced from Eq. 6 are similar to those found from room temperature magnetization curves and follow a similar trend to that shown by the values deduced from TEM, as shown in Table 2 (D_{ZFC}).

3.3 NMR relaxation times

For a preliminary assessment of the SPIONs as MRI contrast agents, the longitudinal (T_1) and transverse (T_2) relaxation times were measured for each sample. First, NMR experiments were performed on 0.43 mM solutions of a series of samples that were selected according with the better stability of the aqueous suspension. For that concentrated suspensions of NP were diluted in nanopure water with a 20% of deuterium oxide, in order to avoid saturation of the proton signal. Figure 5 shows the time plots for the longitudinal magnetization (M_z) recovery and the transverse magnetization (M_{xy}) relaxation measured for some samples selected. The best curve fitting of the experimental results according to Eqs. 1 and 2 are also displayed. It should be pointed out that the most relevant processing parameter for the relaxation behaviour of the samples is the glutathione ratio used. We find that samples with a 1:9 ratio lead to a faster recovery and relaxation, respectively, but the use of different NaOH content (Low, Medium, High) leads to very slight differences in the relaxation process (Fig. 5b). The characteristic relaxation parameters evaluated from the fitting curves of the Fig. 5 are presented in Table 3:

Calculated T_1 times range from 1.7 to 5.9 s and T_2 times vary from 16.1 to 14.4 ms, being in both cases shorter for suspension of NP G9M as pointed out from Fig. 5.

Given that the relaxation rate enhancement is related to the proton diffusion through the magnetic gradient due to the nanoparticles, the larger TE, the longer will be the path through different environments inducing coherence loss between them. Then, the faster the relaxation process would be expected for TE = 2 ms. However, no significant differences are showed between transverse times measured with 1 ms and 2 ms echo time, for the same sample.

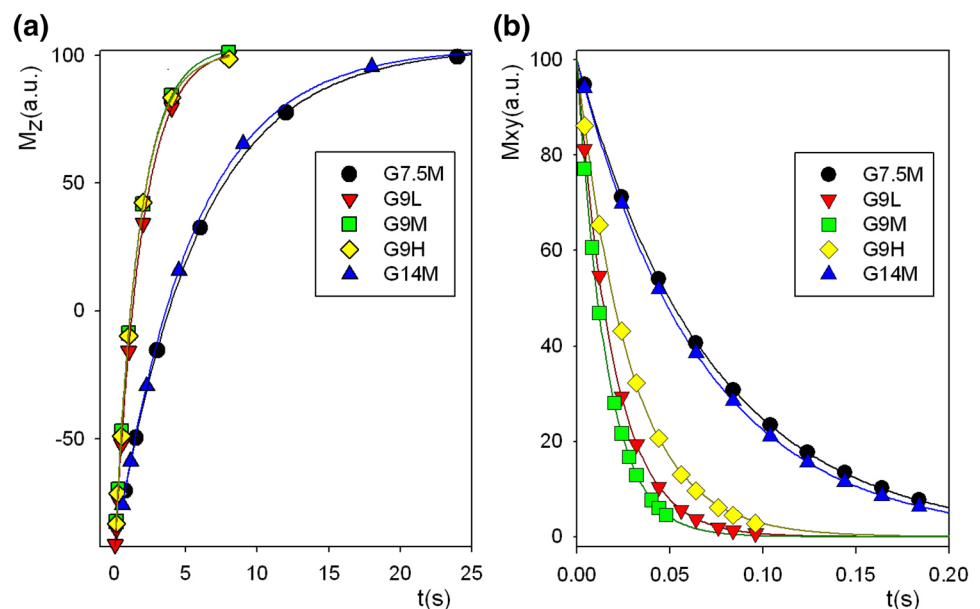
Table 3 also shows the inhomogeneous relaxing time, estimated from the FWHM of the $^1\text{H-NMR}$ signal, which was measured both with the probe stopped (T_{2s}^*) and spinning at 20 Hz (T_{2s}^*) for homogenization. Thus, comparison of these two values gives us an indication of the suspension uniformity in the probe. Additionally, the ratio between T_{2s}^* and T_2 tell us about the significance of the local field inhomogeneities on the transverse relaxation. Comparison of data in the Table 3 for the different samples reveals that these parameters are similar for the solutions of nanoparticles synthesized with a 1/9 GSH ratio

Table 3 Magnetic relaxation times calculated for selected samples: T_1 is the longitudinal relaxation time calculated from magnetization recovery, T_2 is the transverse relaxation time calculated from magnetization decay for 1 ms (TE1) and 2 ms (TE2) echo time

Sample	T_1 (s)	T_{2s}^* (ms)	T_2^* (ms)	T_2 (ms) _{TE2}	T_2 (ms) _{TE1}
G7.5 M	5.85	9.1	9.5	70.6	70.9
G9L	1.87	15.7	15.4	19.72	19.90
G9M	1.71	13.9	13.8	15.9	16.1
G9H	1.66	20.7	20.3	29.1	29.4
G14M	5.45	12.9	16.0	67.39	74.4

T_{2s}^* and T_2^* are the inhomogeneous relaxing times measured with the probe spinning and stationary, respectively

Fig. 5 **a** Longitudinal magnetization recovery and **b** transverse magnetization relaxation as a function of time for time for samples (indicated in the legend) processed with diverse NaOH dose and GSH ratio



that, in consequence, should be the more homogeneous. Conversely, solutions of NP with 1:7.5 or 1:15 GSH ratios exhibit larger discrepancies between T_2^* and T_2 mainly. For that reason, sample G9M in particular was used for further relaxation analysis. This sample shows a relevant deviation between the GHS/MGT ratio between ICP measurement and proposed model prediction. This fact can be ascribed to the presence of more than one layer in the GSH crown surrounding the magnetic core. Thermogravimetric analysis of G9M from 60 to 780 °C revealed a 37% total weight loss. This weight loss is in better agreement with the ICP result than the model estimation, then supporting the postulate of multi-layer GSH covering.

Figure 6 shows the 1 $\mu\text{m} \times 1 \mu\text{m}$ AFM image of the sample G9M and the size distribution obtained from a set of similar AFM images. This distribution shows an average size larger than the one obtained from TEM images. This difference in the estimation of the NPs size is probably due to the fact that the GSH capping surrounding the magnetite cores does not show contrast enough to be visible in TEM images. Then, the TEM size is essentially the magnetite core size. Further characterization of the G9M sample led us to analyze the hydrodynamic size distribution by DLS technique (shown in Fig. 7). The fitting of the experimental data to a lognormal function, provides an average hydrodynamic size of 66.6 nm (Fig. 7). As expected, the hydrodynamic size of NPs, determined by the DLS technique, is significantly higher in comparison with the one obtained by TEM or AFM. This effect is not only assigned to the GSH layer, but also to the presence of extra hydrate layers in aqueous medium. In addition, some agglomeration of the nanoparticles in aqueous solutions is expected due to the magnetism of magnetite NPs [49]. However, this average

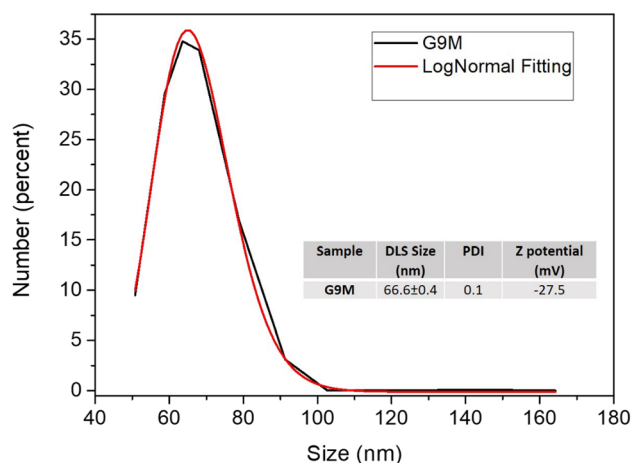


Fig. 7 Hydrodynamic size distribution by DLS technique for sample G9M

hydrodynamic size indicates a colloidal stability appropriate for biomedical applications, corroborated by the PDI value (inset) that evidences a low-moderate dispersion; and by the relatively high value of the Z-potential. In addition, the negative value of the Z-potential suggests that the GSH carboxylic groups are rather oriented outward.

The effect of the excess of GSH surrounding the cores on the relaxation processes was evaluated by the comparison of samples after a number of final washing cycles with PBS. In particular, we investigated the relaxation processes in solutions of G9M NPs processed with 0, 2 and 4 washing cycles. Additionally, we studied the effect of performing a final washing step in distilled water (indicated as + 1 at the end of the sample code).

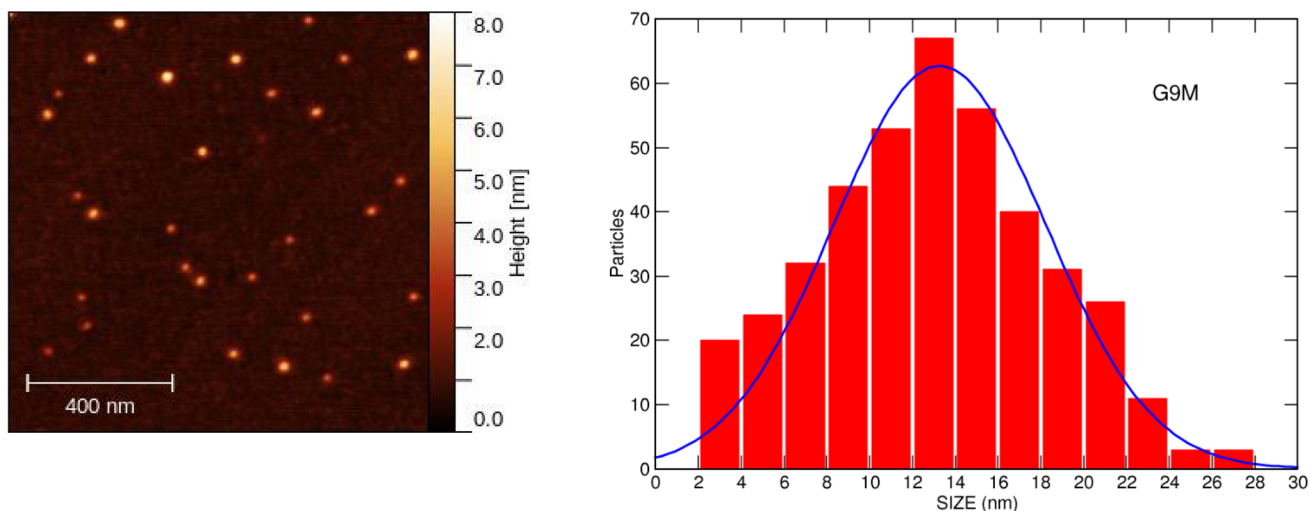
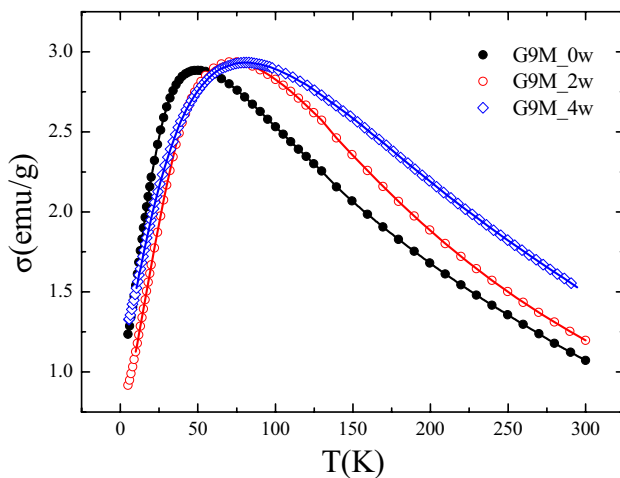


Fig. 6 1 $\mu\text{m} \times 1 \mu\text{m}$ AFM image of G9M sample and size distribution obtained from a set of AFM images

Table 4 Relaxation parameters of sample G9M subjected to *n* washing cycles in PBS, as indicated in the code by G9M_nw

Code	T_1 (s)	T_2^* (ms)	T_2 (ms) _{TE2}	T_2 (ms) _{TE1}
G9M_0w	1.75	8.1	9.7	9.8
G9M_2w	3.48	5.5	21.4	23.4
G9M_4w	3.54	22.7	245	302
G9M_3w+1	5.45	19.0	610	819
G9M_4w+1	5.83	31.3	567	814

Samples processed with a final washing in water (+1) are also included

**Fig. 8** ZFC curves for G9M samples processed with 0, 2 and 4 washing cycles

The characteristic relaxation times for this series are collected in Table 4.

It can be inferred from the results that, on washing the sample, the relaxation behaviour is worsen, since the relaxation rates decrease, particularly $1/T_2$. This trend is even more accentuated when the final washing step in distilled water is done. The effect can be related with a decrease of the NP stability in aqueous-suspension with the washing steps number, as it is revealed by the strong divergences between T_2 and T_2^* and a major effect of the echo time used. This term was confirmed by ICP analysis of the NMR solutions that showed a lower NPs concentration than expected as a consequence of its partial precipitation during the experiment.

At this point, the analysis of the constant-field $M(T)$ experiments may be of help to explain this behaviour. Figure 8 shows the ZFC curves for G9M samples processed with 0, 2 and 4 washing cycles. As the number of washing cycles increases, the blocking temperatures also increase, as a consequence of the enhancement of

the interparticle interactions [50] when the GSH capping layer is reduced.

In view of these results, we selected sample G9M_0w from those analysed as more suitable for a first relaxivity measurement in aqueous medium, as a preliminary evaluation of its efficiency as a contrast agent. Relaxivity (r_i) measures the increase of the water (longitudinal or transverse) relaxation rate when 1 mM of paramagnetic (superparamagnetic, in our case) substance is present. Thus, for the estimation of the relaxivity of our sample, we analysed the effect of NPs concentration on the relaxation rate, using different concentration ranges. As a general trend, we found a strong decrease of both longitudinal and transverse relaxation times with the superparamagnetic component in any case, as it was expected.

For the estimation of relaxivities of NPs, as an evaluation of its performance as a contrast agent for MRI applications, we measured the evolution of the relaxation rates ($1/T_1$ and $1/T_2$) with the NPs concentration in the solution according to:

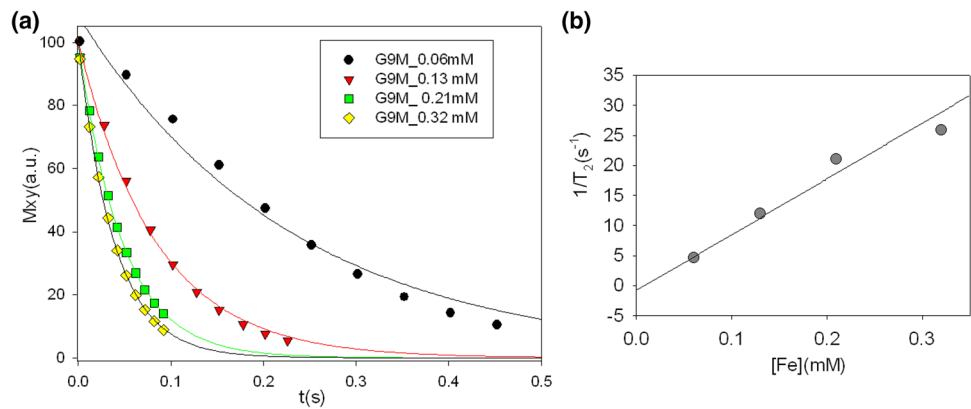
$$\frac{1}{T_i} = \frac{1}{T_{i,w}} + [c]r_i (i = 1, 2) \quad (11)$$

We observed that the slope of this linear trend changes depending on the range of concentration analysed. In fact, a slope change was found for a concentration near 0.2 mM, which has been also found for other samples studied. Consequently, for the relaxivities estimation, we choose a compositional series in the lower concentration range, ranging from 0.06 to 0.32 mM, which would be more adequate for biomedical applications, in order to minimize toxicity effects. Figure 9a presents the relaxation plots for the different concentrations of G9M NPs, as indicated in the legend, measured with $TE = 2$ ms. It is evident that, as NPs concentration increases, transverse relaxation gets faster. In fact, the plot of the resultant transversal relaxation rate versus Fe concentration (Fig. 9b) follows a linear trend in this range. From the slope of this linear fit, a transverse relaxivity of $92.7 \text{ mM}^{-1} \text{ s}^{-1}$ is found. This value is in good agreement with those reported for similar systems [51].

4 Conclusions

This work shows a one-pot chemical route for the synthesis of GSH capped iron oxide NPs to be used as a contrast agent in MRI. Nanoparticles thus obtained exhibit homogenous sizes below 10 nm and a hydrophilic behavior. Moreover, NPs size can be easily tuned by means of the synthesis parameters, and a clear increase of the NPs size is found when a larger amount of the oxidizing agent (NaOH) was added for precipitation. The

Fig. 9 **a** Transversal magnetic relaxation of different solutions of G9M NPs with the concentration indicated in the legend. **b** Relation between transversal relaxation rate ($1/T_2$) and NPs concentration



potential use of these NPs as contrast agents was evaluated through their magnetic behavior and by means of their magnetic relaxation kinetics. The sample that would show the best performance as an MRI contrast agent (i.e., the one with the lowest relaxation times), has a magnetite core size of 6 nm and a GSH weight percentage larger than 40%. This more populated GSH capping layer, together with the small core size, leads to a stable NPs aqueous suspension where interactions between NPs are minimized, producing a homogeneous magnetic environment. As an additional proof of these conclusions, the effect of reducing the GSH content in the capping layer by washing the NPs with PBS, was analyzed. This reduction leads to an increase in relaxation times and superparamagnetic blocking temperatures, which are related to a poorer stability of the dispersions and to the appearance of more intense interparticle interactions, respectively.

Acknowledgements The authors acknowledge the financial support of the Innovation and Science Ministry (PN/PETRI/PR/2007-019) and the Ministry of Economics and Competitiveness (PI16/00784). We would like to thank the Core Science and Technology Research Facility of the University of Cadiz for the use of core infrastructure.

Author contributions J. J. Beato-López. performed all chemical synthesis, TEM characterization and magnetic measurements of prepared samples and interpretation of structural characterization. M. Dominguez. took part in AFM characterization of samples and the interpretation of magnetic measurements. M. Ramírez del.Solar performed measurements related with NMR and in its interpretation. R. Litrán. carried out in XRD measurements, and performed the interpretation of the effect of reagents in subsequent properties of NPS, in the interpretation of ICP results and effect of GSH in solubility and finally in the writing of the paper.

Funding This research was supported by the Innovation and Science Ministry (PN/PETRI/PR/2007-019) and the Ministry of Economics and Competitiveness (PI16/00784) of the government of Spain.

Availability of data and materials The datasets used and/or analysed during the current study are available from the corresponding author on reasonable request.

Compliance with ethical standards

Conflict of interest The authors declare that they have no conflict of interest.

References

- Assa F, Jafarizadeh-Malmiri H, Ajamein H, Anarjan N, Vaghari H, Sayyar Z, Berenjani A (2016) A biotechnological perspective on the application of iron oxide nanoparticles. *Nano Res* 9(8):2203–2225. <https://doi.org/10.1007/s12274-016-1131-9>
- Bagheri S, Julkapli NM (2016) Modified iron oxide nanomaterials: functionalization and application. *J Magn Magn Mater* 416:117–133. <https://doi.org/10.1016/j.jmmm.2016.05.042>
- Karimzadeh I, Dizaji HR, Aghazadeh M (2016) Development of a facile and effective electrochemical strategy for preparation of iron oxides (Fe₃O₄ and gamma-Fe₂O₃) nanoparticles from aqueous and ethanol mediums and in situ PVC coating of Fe₃O₄ superparamagnetic nanoparticles for biomedical applications. *J Magn Magn Mater* 416:81–88. <https://doi.org/10.1016/j.jmmm.2016.05.015>
- Coppola P, da Silva FG, Gomide G, Paula FLO, Campos AFC, Perzynski R, Kern C, Depeyrot J, Aquino R (2016) Hydrothermal synthesis of mixed zinc-cobalt ferrite nanoparticles: structural and magnetic properties. *J Nanopart Res*. <https://doi.org/10.1007/s11051-016-3430-1>
- Tanaka M, Knowles W, Brown R, Hondow N, Arakaki A, Baldwin S, Staniland S, Matsunaga T (2016) Biomagnetic recovery and bioaccumulation of selenium granules in magnetotactic bacteria. *Appl Environ Microbiol* 82(13):3886–3891. <https://doi.org/10.1128/aem.00508-16>
- Wang ZH, Chen M, Shu JX, Li Y (2016) One-step solvothermal synthesis of Fe₃O₄@Cu@Cu₂O nanocomposite as magnetically recyclable mimetic peroxidase. *J Alloy Compd* 682:432–440. <https://doi.org/10.1016/j.jallcom.2016.04.269>
- Mirabedini M, Kassaee MZ (2016) Removal of toxic Cr(VI) from water by a novel magnetic chitosan/glyoxal/PVA hydrogel film. *Desalin Water Treat* 57(30):14266–14279. <https://doi.org/10.1080/19443994.2015.1065763>
- Babincova M, Babincova N, Durdik S, Bergemann C, Sourivong P (2016) Silencing by blasting: combination of laser pulse induced stress waves and magnetophoresis for siRNA delivery. *Laser Phys Lett*. <https://doi.org/10.1088/1612-2011/13/6/065601>
- Zverev VI, Pyatakov AP, Shtil AA, Tishin AM (2018) Novel applications of magnetic materials and technologies for medicine.

- J Magn Magn Mater 459:182–186. <https://doi.org/10.1016/j.jmmm.2017.11.032>
10. Lico C, Schoubben A, Baschieri S, Blasi P, Santi L (2013) Nanoparticles in biomedicine: new insights from plant viruses. *Curr Med Chem* 20(28):3471–3487
 11. Kayili HM, Salih B (2016) Fast and efficient proteolysis by reusable pepsin-encapsulated magnetic sol-gel material for mass spectrometry-based proteomics applications. *Talanta* 155:78–86. <https://doi.org/10.1016/j.talanta.2016.04.014>
 12. Chalkidou A, Simeonidis K, Angelakeris M, Samaras T, Martinez-Boubeta C, Balcells L, Papazisis K, Dendrinou-Samara C, Kalogirou O (2011) In vitro application of Fe/MgO nanoparticles as magnetically mediated hyperthermia agents for cancer treatment. *J Magn Magn Mater* 323(6):775–780. <https://doi.org/10.1016/j.jmmm.2010.10.043>
 13. Soares PIP, Ferreira IMM, Igreja R, Novo CMM, Borges J (2012) Application of hyperthermia for cancer treatment: recent patents review. *Recent Pat Anti-Cancer Drug Discov* 7(1):64–73
 14. Kubickova L, Brazda P, Veverka M, Kaman O, Herynek V, Vosmanska M, Dvorak P, Bernasek K, Kohout J (2019) Nanomagnets for ultra-high field MRI: magnetic properties and transverse relaxivity of silica-coated epsilon-Fe₂O₃. *J Magn Magn Mater* 480:154–163. <https://doi.org/10.1016/j.jmmm.2019.02.067>
 15. Zhang M, Wagner MJ (2018) Gadolinium-gold core-shell nanocrystals: potential contrast agents for molecular MRI with high T-1 relaxivity. *J Magn Magn Mater* 454:254–257. <https://doi.org/10.1016/j.jmmm.2018.01.082>
 16. Gharehaghaji N, Divband B, Zareei L (2018) Nanoparticulate NaA zeolite composites for MRI: effect of iron oxide content on image contrast. *J Magn Magn Mater* 456:136–141. <https://doi.org/10.1016/j.jmmm.2018.02.013>
 17. Soares PIP, Laia CAT, Carvalho A, Pereira LCJ, Coutinho JT, Ferreira IMM, Novo CMM, Borges JP (2016) Iron oxide nanoparticles stabilized with a bilayer of oleic acid for magnetic hyperthermia and MRI applications. *Appl Surf Sci* 383:240–247. <https://doi.org/10.1016/j.apsusc.2016.04.181>
 18. Zhang L, Liang S, Liu RQ, Yuan TM, Zhang SL, Xu ZS, Xu HB (2016) Facile preparation of multifunctional uniform magnetic microspheres for T-1-T-2 dual modal magnetic resonance and optical imaging. *Colloids Surfaces B-Biointerfaces* 144:344–354. <https://doi.org/10.1016/j.colsurfb.2016.04.014>
 19. Filippi M, Boido M, Pasquino C, Garello F, Boffa C, Terreno E (2016) Successful in vivo MRI tracking of MSCs labeled with gadoteridol in a spinal cord injury experimental model. *Exp Neurol* 282:66–77. <https://doi.org/10.1016/j.expneurol.2016.05.023>
 20. Wartenberg N, Fries P, Raccurt O, Guillermo A, Imbert D, Mazzanti M (2013) A gadolinium complex confined in silica nanoparticles as a highly efficient T1/T2 MRI contrast agent. *Chem-a Eur J* 19(22):6980–6983. <https://doi.org/10.1002/chem.201300635>
 21. Feng L, Zhu C, Yuan H, Liu L, Lv F, Wang S (2013) Conjugated polymer nanoparticles: preparation, properties, functionalization and biological applications. *Chem Soc Rev* 42(16):6620–6633. <https://doi.org/10.1039/c3cs60036j>
 22. Wu CQ, Li DY, Yang L, Lin BB, Zhang HB, Xu Y, Cheng ZZ, Xia CC, Gong QY, Song B, Ai H (2015) Multivalent manganese complex decorated amphiphilic dextran micelles as sensitive MRI probes. *J Mater Chem B* 3(8):1470–1473. <https://doi.org/10.1039/c4tb02036g>
 23. Courant T, Roullin VG, Cadiou C, Callewaert M, Andry MC, Portefaix C, Hoefel C, de Goltstein MC, Port M, Laurent S, Vander Elst L, Muller R, Molinari M, Chuburu F (2012) Hydrogels incorporating GdDOTA: towards highly efficient dual T1/T2 MRI contrast agents. *Angew Chem-Int Ed* 51(36):9119–9122. <https://doi.org/10.1002/anie.201203190>
 24. Scialabba C, Puleio R, Peddis D, Varvaro G, Calandra P, Cassata G, Cicero L, Licciardi M, Giammona G (2017) Folate targeted coated SPIONs as efficient tool for MRI. *Nano Res* 10(9):3212–3227. <https://doi.org/10.1007/s12274-017-1540-4>
 25. Zhang Q, Rajan SS, Tyner KM, Casey BJ, Dugard CK, Jones Y, Paredes AM, Clingman CS, Howard PC, Goering PL (2016) Effects of iron oxide nanoparticles on biological responses and MR imaging properties in human mammary healthy and breast cancer epithelial cells. *J Biomed Mater Res Part B-Appl Biomater* 104(5):1032–1042. <https://doi.org/10.1002/jbm.b.33450>
 26. Azhdarzadeh M, Atyabi F, Saei AA, Varnamkhasti BS, Omidi Y, Fateh M, Ghavami M, Shanehsazzadeh S, Dinarvand R (2016) Theranostic MUC-1 aptamer targeted gold coated superparamagnetic iron oxide nanoparticles for magnetic resonance imaging and photothermal therapy of colon cancer. *Colloids Surfaces B-Biointerfaces* 143:224–232. <https://doi.org/10.1016/j.colsurfb.2016.02.058>
 27. Kostevsek N, Sturm S, Sersa I, Sepe A, Bloemen M, Verbiest T, Kobe S, Rozman KZ (2015) “Single-” and “multi-core” FePt nanoparticles: from controlled synthesis via zwitterionic and silica bio-functionalization to MRI applications. *J Nanopart Res*. <https://doi.org/10.1007/s11051-015-3278-9>
 28. Jahanbin T, Gaceur M, Gros-Dagnac H, Benderbous S, Merah SA (2015) High potential of Mn-doped ZnS nanoparticles with different dopant concentrations as novel MRI contrast agents: synthesis and in vitro relaxivity studies. *J Nanopart Res*. <https://doi.org/10.1007/s11051-015-3038-x>
 29. Alsmadi NA, Wadajkar AS, Cui W, Nguyen KT (2011) Effects of surfactants on properties of polymer-coated magnetic nanoparticles for drug delivery application. *J Nanopart Res* 13(12):7177–7186. <https://doi.org/10.1007/s11051-011-0632-4>
 30. Soares PIP, Alves AMR, Pereira LCJ, Coutinho JT, Ferreira IMM, Novo CMM, Borges J (2014) Effects of surfactants on the magnetic properties of iron oxide colloids. *J Colloid Interface Sci* 419:46–51. <https://doi.org/10.1016/j.jcis.2013.12.045>
 31. Litran R, Sampedro B, Rojas TC, Multigner M, Sanchez-Lopez JC, Crespo P, Lopez-Cartes C, Garcia MA, Hernando A, Fernandez A (2006) Magnetic and microstructural analysis of palladium nanoparticles with different capping systems. *Phys Rev B*. <https://doi.org/10.1103/physrevb.73.054404>
 32. Sampedro B, Crespo P, Hernando A, Litran R, Lopez JCS, Cartes CL, Fernandez A, Ramirez J, Calbet JG, Vallet M (2003) Ferromagnetism in fcc twinned 2.4 nm size Pd nanoparticles. *Phys Rev Lett*. <https://doi.org/10.1103/physrevlett.91.237203>
 33. Crespo P, Litran R, Rojas TC, Multigner M, de la Fuente JM, Sanchez-Lopez JC, Garcia MA, Hernando A, Penades S, Fernandez A (2004) Permanent magnetism, magnetic anisotropy, and hysteresis of thiol-capped gold nanoparticles. *Phys Rev Lett*. <https://doi.org/10.1103/physrevlett.93.087204>
 34. Beato-Lopez JJ, Fernandez-Ponce C, Blanco E, Barrera-Solano C, Ramirez-del-Solar M, Dominguez M, Garcia-Cozar F, Litran R (2012) Preparation and characterization of fluorescent CdS quantum dots used for the direct detection of GST fusion proteins regular paper. *Nanomater Nanotechnol* 2:10
 35. Beato-Lopez JJ, Espinazo ML, Fernandez-Ponce C, Blanco E, Ramirez-del-Solar M, Dominguez M, Garcia-Cozar E, Litran R (2017) CdTe quantum dots linked to Glutathione as a bridge for protein crosslinking. *J Lumin* 187:193–200. <https://doi.org/10.1016/j.jlumin.2017.03.012>
 36. Fernandez-Ponce C, Munoz-Miranda JP, de los Santos DM, Aguado E, Garcia-Cozar F, Litran R (2018) Influence of size and surface capping on photoluminescence and cytotoxicity of gold nanoparticles. *J Nanopart Res* 20:11. <https://doi.org/10.1007/s11051-018-4406-0>
 37. Teng Y, Pong PWT (2018) One-pot synthesis and surface modification of lauric-acid-capped CoFe₂O₄ nanoparticles. *IEEE Trans Magn* 54:11. <https://doi.org/10.1109/tmag.2018.2834524>

38. Rashid H, Mansoor MA, Haider B, Nasir R, Abd Hamid SB, Abdulrahman A (2020) Synthesis and characterization of magnetite nano particles with high selectivity using in situ precipitation method. *Sep Sci Technol* 55(6):1207–1215. <https://doi.org/10.1080/01496395.2019.1585876>
39. Yu X, Cheng G, Zheng S-Y (2016) Synthesis of self-assembled multifunctional nanocomposite catalysts with highly stabilized reactivity and magnetic recyclability. *Sci Rep*. <https://doi.org/10.1038/srep25459>
40. Necas D, Klapetek P (2012) Gwyddion: an open-source software for SPM data analysis. *Cent Eur J Phys* 10(1):181–188. <https://doi.org/10.2478/s11534-011-0096-2>
41. Meiboom S, Gill D (1958) Modified spin-echo method for measuring nuclear relaxation times. *Rev Sci Instrum* 29(8):688–691. <https://doi.org/10.1063/1.1716296>
42. Hermosa G, Chen W-C, Wu H-S, Liao C-S, Sun Y-M, Wang S-F, Chen Y, Sun A-C (2020) Investigations of the effective parameters on the synthesis of monodispersed magnetic Fe₃O₄ by solvothermal method for biomedical applications. *AIP Adv*. <https://doi.org/10.1063/1.5130063>
43. Scardi P, Leoni M (2001) Diffraction line profiles from polydisperse crystalline systems. *Acta Crystallogr Sect A* 57:604–613. <https://doi.org/10.1107/s0108767301008881>
44. Scilab Enterprises (2012) Scilab: free and open source software for numerical computation, Versailles, Ile-de-France, France
45. Dormann JL, Fiorani D, Tronc E (1997) Magnetic relaxation in fine-particle systems. In: Prigogine I, Rice SA (eds) *Advances in chemical physics*, vol 98. Wiley, Hoboken. <https://doi.org/10.1002/9780470141571>
46. Chikazumi S (2019) *Phys Magn* 145:260. Clarendon press, Oxford
47. Vargas JM, Lima E Jr, Zysler RD, Duque JGS, De Biasi E, Knobel M (2008) Effective anisotropy field variation of magnetite nanoparticles with size reduction. *Eur Phys J B* 64(2):211–218. <https://doi.org/10.1140/epjb/e2008-00294-6>
48. Lisjak D, Mertelj A (2018) Anisotropic magnetic nanoparticles: a review of their properties, syntheses and potential applications. *Prog Mater Sci* 95:286–328. <https://doi.org/10.1016/j.pmatsci.2018.03.003>
49. Santos MC, Seabra AB, Pelegrino MT, Haddad PS (2016) Synthesis, characterization and cytotoxicity of glutathione- and PEG-glutathione-superparamagnetic iron oxide nanoparticles for nitric oxide delivery. *Appl Surf Sci* 367:26–35. <https://doi.org/10.1016/j.apsusc.2016.01.039>
50. Garcia-Otero J, Porto M, Rivas J, Bunde A (2000) Influence of dipolar interaction on magnetic properties of ultrafine ferromagnetic particles. *Phys Rev Lett* 84(1):167–170. <https://doi.org/10.1103/PhysRevLett.84.167>
51. Faucher L, Gossuin Y, Hocq A, Fortin M-A (2011) Impact of agglomeration on the relaxometric properties of paramagnetic ultra-small gadolinium oxide nanoparticles. *Nanotechnology*. <https://doi.org/10.1088/0957-4484/22/29/295103>

Publisher's Note Springer Nature remains neutral with regard to jurisdictional claims in published maps and institutional affiliations.